

Redox Potentials of Colloidal n-Type ZnO Nanocrystals: Effects of Confinement, Electron Density, and Fermi-Level Pinning by Aldehyde Hydrogenation

Gerard M. Carroll, Alina M. Schimpf, Emily Y. Tsui, and Daniel R. Gamelin

J. Am. Chem. Soc., **Just Accepted Manuscript** • Publication Date (Web): 11 Aug 2015

Downloaded from <http://pubs.acs.org> on August 12, 2015

Just Accepted

"Just Accepted" manuscripts have been peer-reviewed and accepted for publication. They are posted online prior to technical editing, formatting for publication and author proofing. The American Chemical Society provides "Just Accepted" as a free service to the research community to expedite the dissemination of scientific material as soon as possible after acceptance. "Just Accepted" manuscripts appear in full in PDF format accompanied by an HTML abstract. "Just Accepted" manuscripts have been fully peer reviewed, but should not be considered the official version of record. They are accessible to all readers and citable by the Digital Object Identifier (DOI®). "Just Accepted" is an optional service offered to authors. Therefore, the "Just Accepted" Web site may not include all articles that will be published in the journal. After a manuscript is technically edited and formatted, it will be removed from the "Just Accepted" Web site and published as an ASAP article. Note that technical editing may introduce minor changes to the manuscript text and/or graphics which could affect content, and all legal disclaimers and ethical guidelines that apply to the journal pertain. ACS cannot be held responsible for errors or consequences arising from the use of information contained in these "Just Accepted" manuscripts.



Redox Potentials of Colloidal *n*-Type ZnO Nanocrystals: Effects of Confinement, Electron Density, and Fermi-Level Pinning by Aldehyde Hydrogenation

Gerard M. Carroll, Alina M. Schimpf, Emily Y. Tsui, and Daniel R. Gamelin*

Department of Chemistry, University of Washington, Seattle, WA 98195-1700, USA

*Electronic address: Gamelin@chem.washington.edu

Abstract. Electronically doped colloidal semiconductor nanocrystals offer valuable opportunities to probe the new physical and chemical properties imparted by their excess charge carriers. Photodoping is a powerful approach to introducing and controlling free carrier densities within free-standing colloidal semiconductor nanocrystals. Photoreduced (*n*-type) colloidal ZnO nanocrystals possessing delocalized conduction-band (CB) electrons can be formed by photochemical oxidation of EtOH. Previous studies of this chemistry have demonstrated photochemical electron accumulation, in some cases reaching as many as >100 electrons per ZnO nanocrystal, but in every case examined to date this chemistry maximizes at a well-defined average electron density of $\langle N_{\text{max}} \rangle = \sim 1.4 \pm 0.4 \times 10^{20} \text{ cm}^{-3}$. The origins of this maximum have never been identified. Here, we use a solvated redox indicator for *in situ* determination of reduced ZnO nanocrystal redox potentials. The Fermi levels of various photodoped ZnO nanocrystals possessing on average just one excess CB electron show quantum-confinement effects, as expected, but are >600 meV lower than those of the same ZnO nanocrystals reduced chemically using Cp^*_2Co , reflecting important differences between their charge-compensating cations. Upon photochemical electron accumulation, the Fermi levels become independent of nanocrystal volume at $\langle N \rangle$ above $\sim 2 \times 10^{19} \text{ cm}^{-3}$, and maximize at $\langle N_{\text{max}} \rangle = \sim 1.6 \pm 0.3 \times 10^{20} \text{ cm}^{-3}$. This maximum is proposed to arise from Fermi-level pinning by the two-electron two-proton hydrogenation of acetaldehyde, which reverses the EtOH photooxidation reaction.

Introduction

Photodoping offers a convenient method for tuning carrier densities in colloidal semiconductor nanocrystals. Photochemical *n*-doping to yield excess delocalized band-like electrons has been studied for a variety of colloidal nanocrystals including ZnO,¹⁻⁶ In₂O₃,⁷ and CdE (E = S, Se, Te),⁸ and with a variety of hole quenchers.⁶ The most thoroughly investigated system has been colloidal ZnO nanocrystals reduced using ethanol (EtOH) as the hole quencher.^{1,3-6} Upon nanocrystal photoexcitation, an electron is excited from the valence band (VB) to the conduction band (CB). The photogenerated hole is then quenched within picoseconds,⁹ leaving the electron in the ZnO CB. EtOH oxidation liberates protons (H⁺) that compensate the CB electron charges, with acetaldehyde as the two-electron two-proton oxidation product^{10,11} according to the stoichiometry of eq 1.



In this system, multiple delocalized CB electrons per ZnO nanocrystal can be accumulated photochemically, with the average ($\langle n \rangle$) reaching as high as >100 in some cases.⁶ Under rigorously anaerobic conditions, the CB electrons are stable after terminating the nanocrystal photoexcitation,⁵ making these *n*-doped ZnO nanocrystals well suited for further spectroscopic or chemical investigations. The average maximum number of electrons per nanocrystal ($\langle n_{\text{max}} \rangle$) was found to be proportional to nanocrystal volume, such that the average maximum electron *density* is constant for all sizes at $\langle N_{\text{max}} \rangle = \sim 1.4 \times 10^{20} \text{ cm}^{-3}$ for ZnO photodoped using EtOH.⁶ The microscopic origin of this maximum remains unidentified, and both kinetic and thermodynamic limitations to further electron accumulation can be postulated.^{2,6}

Photoluminescence measurements^{12,13} and electron-transfer chemistries^{14,15} provide strong evidence that the potentials of CB electrons in colloidal ZnO nanocrystals are subject to

quantum confinement effects, but these measurements have only probed the limit of $\langle n \rangle = 1$. The ability to accumulate tens to hundreds of excess CB electrons per nanocrystal *via* photodoping raises intriguing questions about how to describe the redox potentials and Fermi levels (E_F) of such heavily reduced ZnO nanocrystals, and the dependence of these parameters on the method of reduction.

Here, we report contactless *in situ* determination of the redox potentials of *n*-type colloidal ZnO nanocrystals using an optical redox indicator. The data show that E_F is subject to quantum confinement effects in the limit of one electron per nanocrystal, as anticipated from prior results. With further electron accumulation, however, E_F becomes independent of quantum confinement and depends only on electron density. E_F is shown to depend strongly on the identity of the charge-compensating cation, spanning a range of ~ 600 meV when only one electron per nanocrystal is present, consistent with previous reactivity studies.¹⁶ $\langle N_{\max} \rangle$ and E_F^{\max} are found to be determined by electron Fermi-level pinning, which occurs at the same potential for all nanocrystal sizes. Aldehyde hydrogenation, *i.e.*, the two-electron two-proton reaction that reverses the EtOH photooxidation, is proposed to be the microscopic origin of this Fermi-level pinning.

Methods

ZnO nanocrystal synthesis. Colloidal ZnO nanocrystals were synthesized by base-initiated hydrolysis and condensation of Zn^{2+} as detailed previously.^{17,18} In a typical synthesis, a solution of 22 mmol of TMAH in 40 mL of EtOH was added drop wise to a stirred solution of 13 mmol of $\text{Zn}(\text{OAc})_2$ in 135 mL of DMSO at room temperature. Nanocrystals were grown for ~ 1 hr, after which the reaction was stopped by precipitation with 300 mL of ethyl acetate. Nanocrystals were collected via centrifugation and resuspended in EtOH, followed by

precipitation with heptane. To suspend the nanocrystals in nonpolar solvents, the surface ligands were exchanged by suspending the nanocrystals in excess of dodecylamine (DDA) that had been heated above the melting point (29 °C), followed by precipitation with EtOH. Finally, the nanocrystals were heated in trioctylphosphine oxide (TOPO, 90%) at 130 °C for 30 min. The resulting TOPO-capped nanocrystals were then washed with 3:1 EtOH/toluene and resuspended in toluene. The largest ZnO nanocrystals were made in a similar manner but were heated under N₂ in DDA at 180 °C for ~24 h prior to TOPO capping to promote growth to various sizes.

Physical characterization. UV-Vis-NIR absorption spectra were collected in a 1 cm air-free quartz cuvette using a Cary 500 spectrometer, with typical nanocrystal concentrations of 5-20 μM. The radii of small nanocrystals ($r \leq 2.8$ nm) were determined from the empirical correlation between radii and absorption spectra.^{13,19} The radii of larger nanocrystals ($r = 3.7$ nm) were determined by statistical analysis of transmission electron microscope (TEM) images collected using a FEI Tecnai G2 F20. ZnO nanocrystal concentrations were determined analytically. 200 μL of the nanocrystal suspension was dried and digested in 200 μL of ultrapure nitric acid (TraceSELECT, Fluka). The resulting solution was diluted with a known amount of ultrapure water (10.00 g, measured to two decimal places on a balance), and the Zn²⁺ concentration was measured using inductively coupled plasma atomic emission spectroscopy (Perkin-Elmer 8300). The nanocrystal concentration was then calculated using the known dilution factors and nanocrystal radii to convert from Zn²⁺ concentration to nanocrystal concentration.

Photodoping. ZnO nanocrystals were suspended in dry, anaerobic toluene/THF (1:14) solutions and prepared in a 1 cm air-free cuvette, then photodoped to their maximum level by prolonged exposure to UV irradiation from a 100 W Hg/Xe Oriel broad-band photolysis lamp (2

W/cm², 1.5 cm illumination diameter) in the presence of EtOH and [Cp₂Co][PF₆] (0.233–0.633 mM). THF was used to aid the solubility of [Cp₂Co][PF₆]. The UV-Vis-NIR absorption was collected periodically during the photodoping process. When the NIR absorption did not change over 20 min of UV exposure, the nanocrystals were considered to have reached their maximum photodoping level. Maximum photodoping was typically achieved within 90 min of UV irradiation.

Electron counting by titration. The average number of photodoped electrons per ZnO nanocrystal ($\langle n \rangle$) was determined by titration with [FeCp*₂][BAr_F] (Figure S1).^{6,20,21} Aliquots of [FeCp*₂][BAr_F] in THF were added to the maximally photodoped nanocrystals and the reduction of the NIR absorption was monitored. After complete elimination of the NIR absorption, additional aliquots led to growth of FeCp*₂⁺ absorption centered at 700 nm. The data were then fit with a linear function and the maximum number of photodoped electrons was determined from the x-intercept of the fitted line.

Electron counting from NIR absorption. The average number of electrons per nanocrystal, $\langle n \rangle$, was determined spectroscopically from the NIR absorption involving intraband transitions of the CB electrons. For this, molar extinction coefficients (ϵ) were determined for each ZnO nanocrystal size at five different wavelengths (500, 778, 1000, 1300, and 1600 nm) and at various values of $\langle n \rangle$, by [FeCp*₂][BAr_F] titration. These ϵ values were fit to a power function with the general form $\epsilon_\lambda = Q_\lambda \times \langle n \rangle^p$ (Figure S1b), where Q (M⁻¹ cm⁻¹ electron⁻¹) and p (unitless) are constants. Substitution into the Beer's-law equation and rearranging for $\langle n \rangle$, the expression becomes $\langle n \rangle = \text{Abs}_\lambda \times \exp(p) \times Q_\lambda^{-1} \times b^{-1} \times C^{-1}$, where b is the optical pathlength (cm) and C is the concentration (M). Values of $\langle n \rangle$ calculated from the absorption at 778, 1000, 1300, and 1600 nm were averaged together to obtain the reported values of $\langle n \rangle$, with error

bars reported as $\pm\sigma$ from the mean value of $\langle n \rangle$. The $\langle n \rangle$ values reported here were measured without UV illumination. Under these conditions, $\langle n \rangle$ is constant.

Optical Fermi-level measurements. Fermi levels (E_F) were measured using Cp_2Co as an *in situ* optical redox indicator. Measurements of E_F were performed in the absence of UV photoexcitation. Under these conditions, $\langle n \rangle$ and E_F are stable. Cp_2Co concentrations were measured spectroscopically using the absorption feature at 500 nm ($\epsilon_{500} = 301 \text{ M}^{-1}\text{cm}^{-1}$),²² accounting for overlapping ZnO intraband absorption. Cp_2Co concentrations were then determined using Beer's law, and E_F was calculated from the Nernst equation. The E_F values reported here are thus equilibrium values measured without UV illumination and are stable under rigorously anaerobic conditions.

Results and Analysis

Figure 1a plots electronic absorption spectra of colloidal ZnO nanocrystals ($r = 1.9 \text{ nm}$) collected at various stages of nanocrystal photodoping using EtOH as the hole quencher. In these measurements, $[\text{Cp}_2\text{Co}][\text{PF}_6]$ ($\text{Cp}_2\text{Co}^+ = \text{cobaltocenium}$, $\text{PF}_6^- = \text{hexafluorophosphate}$) has been added to the reaction mixture for use as an optical redox indicator. As detailed previously, photodoping leads to bleaching of the ZnO band-edge absorption (inset) and growth of a comparably intense IR intra-band absorption feature, both indicating a growing population of delocalized CB electrons (e^-_{CB}).^{1-3,5,6,14-16,23-26} The IR absorbance can be analyzed to provide the average number of electrons per ZnO nanocrystal ($\langle n \rangle$) at each level of photodoping. In the present experiments, new absorption features at 390 and 500 nm are also observed upon photodoping, attributable to the LMCT and $d-d$ transitions of cobaltocene (Cp_2Co), respectively.²² The concentration of Cp_2Co is determined from the Cp_2Co absorbance at 500 nm and its extinction coefficient ($\epsilon_{500} = 301 \text{ M}^{-1}\text{cm}^{-1}$) using Beer's law. Using the Nernst equation

(eq 2) and the experimental Cp₂Co redox potential ($E^{\circ} = -1.37$ V vs Fc⁺/Fc, see Supporting Information), the solution potential (E_{cell}) may then be calculated. As measured by the quotient [Cp₂Co]/[Cp₂Co⁺], E_{cell} directly reports the electron Fermi level (E_{F}) of the ensemble of ZnO nanocrystals,^{27,28} which are in thermodynamic equilibrium with the Cp₂Co⁺/Cp₂Co couple. The solution potential therefore equals the ZnO electron Fermi level.

$$E_{\text{F}}(V) = E_{\text{cell}}(V) = E^{\circ} - 0.02568 \times \ln \frac{[\text{Cp}_2\text{Co}]}{[\text{Cp}_2\text{Co}^+]} \quad (2)$$

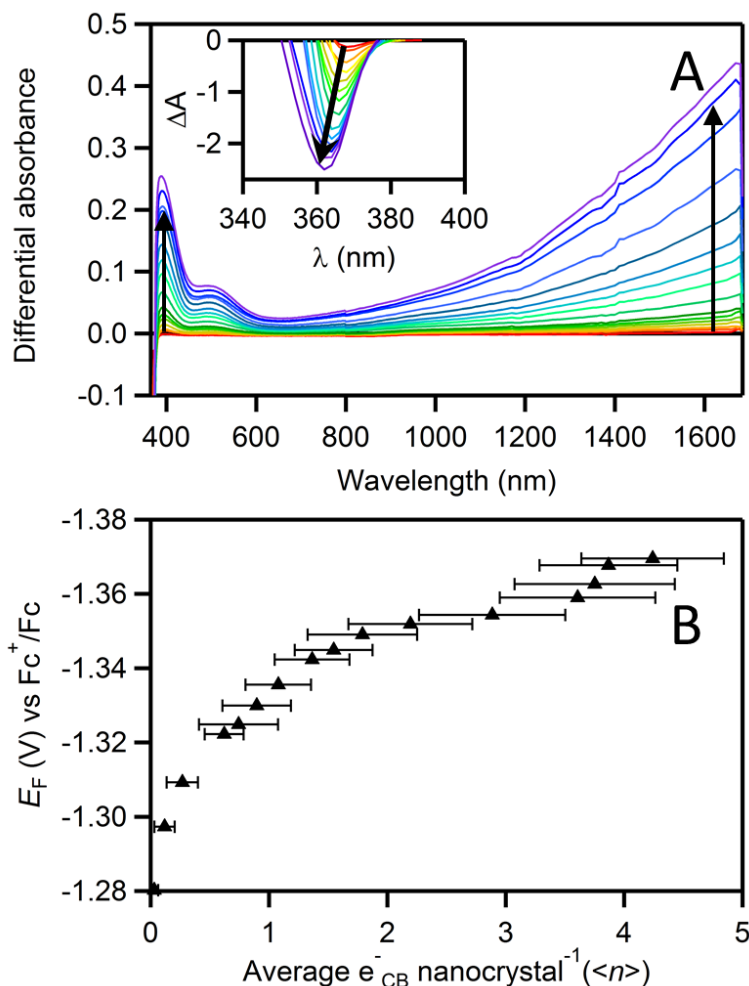


Figure 1. (A) Representative differential electronic absorption spectra collected at various illumination times between 0 and 1 hr during photochemical reduction of 9.45 μM colloidal ZnO ($r = 1.9$ nm) nanocrystals in the presence of 466 μM $[\text{Cp}_2\text{Co}][\text{PF}_6]$ in a 14:1:0.5 THF/toluene/ethanol mixture. The main panel shows the visible spectral range, and the inset shows the UV (ZnO interband) range. Note the different y-axis scaling. The arrows indicate the direction of increased photodoping. (B) Plot of electron Fermi level (E_F , black triangles) vs average number of CB electrons per nanocrystal ($\langle n \rangle$), calculated from the Cp_2Co absorbance at $\lambda = 500$ nm ($\epsilon_{500} = 301 \text{ M}^{-1}\text{cm}^{-1}$) at each stage of photodoping. E_F values are referenced to the ferrocenium/ferrocene (Fc^+/Fc) redox couple. The error bars indicate $\pm\sigma$ from the mean value of $\langle n \rangle$. The quotient $[\text{Cp}_2\text{Co}]/([\text{Cp}_2\text{Co}] + [\text{Cp}_2\text{Co}^+])$ is ~ 0.5 at $\langle n_{\text{max}} \rangle$ in these measurements.

Figure 1b plots E_F vs $\langle n \rangle$ for the entire data set of Figure 1a. Initially, mixing undoped ZnO nanocrystals with Cp_2Co^+ yields no detectable Cp_2Co , indicating that E_F of the undoped ZnO nanocrystals is far more positive than -1.37 V (the $\text{Cp}_2\text{Co}^+/\text{Cp}_2\text{Co}$ redox couple). Upon UV

photoexcitation of this mixture, E_F increases rapidly in concert with ZnO photodoping, growing from -1.28 to ~ -1.35 V, where its value levels off until $\langle n \rangle \sim 3.7$, at which point E_F increases sharply to reach its maximum value of $E_F^{\max} \sim -1.37$ V at $\langle n \rangle = 4.3$. This value of $\langle n \rangle$ is the maximum number of electrons ($\langle n_{\max} \rangle$) that can be introduced under these conditions.⁶ Further UV irradiation yields no change in $\langle n \rangle$ or E_F . The full range of E_F in these data is ~ 90 meV, smaller than the ~ 350 meV range measured in electrochemical ZnO nanocrystal reduction experiments.²⁹ This difference is in large part due to the absence of an E_F data point prior to photodoping, and it may also relate to the different counterions of the two measurements (*vide infra*).

Measurements under the same photodoping conditions but using different Cp_2Co^+ concentrations all yield the same values of E_F vs $\langle n \rangle$ (see Supporting Information). Additionally, when the weaker oxidant decamethylcobaltocenium (Cp^*Co^+ , $E^\circ = -1.91$ V vs Fc/Fc^+ in MeCN ³⁰) is added instead of Cp_2Co^+ , no formation of decamethylcobaltocene (Cp^*Co) is observed (see Supporting Information). Together, these results confirm that the $\text{Cp}_2\text{Co}^+/\text{Cp}_2\text{Co}$ redox couple is indeed in equilibrium with the ZnO nanocrystals.

We have previously reported that $\langle n_{\max} \rangle$ in photodoped ZnO nanocrystals scales with nanocrystal volume,⁶ but the fundamental origins of this scaling have not been identified. It is possible that $\langle n \rangle$ is limited kinetically, for example by the lifetimes of photogenerated holes, but it is also possible that $\langle n \rangle$ is limited thermodynamically, for example by reductive metallization of the ZnO nanocrystals at high carrier densities.⁶ To address this issue, we have used this redox-indicator method to measure changes in E_F with changes in $\langle n \rangle$ for ZnO nanocrystals of three different sizes, and the results are summarized in Figure 2. From Figure 2a, the largest ZnO nanocrystals ($r = 3.7$ nm) show the least negative E_F value at $\langle n \rangle = 1$, followed by the

intermediate ($r = 2.8$ nm) and then the smallest ($r = 1.9$ nm) nanocrystals. From the optical bandgap energies of this series of nanocrystals (see Supporting Information) and the optically deduced ratio of CB-to-bandgap shifts with quantum confinement,^{12,15} the CB energy is predicted to shift negatively by ~ 76 meV going from $r = 3.7$ to 1.9 nm. In good agreement with this prediction, the data in Figure 2a show a shift of ~ 60 meV at $\langle n \rangle = 1$, the two values being indistinguishable within the uncertainty in $\langle n \rangle$ ($\sigma = \pm 0.2$ electrons at $\langle n \rangle = 1$). The effect of quantum confinement on E_F in the one-electron limit is thus well understood from optical studies. Beyond $\langle n \rangle = 1$, the plots of E_F vs $\langle n \rangle$ in Figure 2a all show similar asymptotic curvature, and notably, each curve plateaus at a similar potential near -1.37 V. Figure 2b plots the same E_F data vs average electron density ($\langle N \rangle$). Remarkably, all three curves are now superimposable within experimental uncertainty. E_F increases by < 25 meV going from $\langle N \rangle = 2 \times 10^{19} \text{ cm}^{-3}$ to $5 \times 10^{19} \text{ cm}^{-3}$, which agrees well with previously reported values for electron-electron repulsion in ZnO nanocrystals with H^+ counter ions.³¹ Like $\langle N_{\text{max}} \rangle$, E_F^{max} is thus also independent of nanocrystal size for a given hole quencher. For all three nanocrystal sizes, E_F maximizes near -1.37 V at $\langle N_{\text{max}} \rangle = \sim 1.6 \pm 0.3 \times 10^{20} \text{ cm}^{-3}$. The data in Figure 2 provide a strong indication of Fermi-level pinning during nanocrystal photodoping. This result points to the conclusion that $\langle N_{\text{max}} \rangle$ in photodoped ZnO nanocrystals is determined specifically by the electron Fermi level, rather than by kinetic limitations.

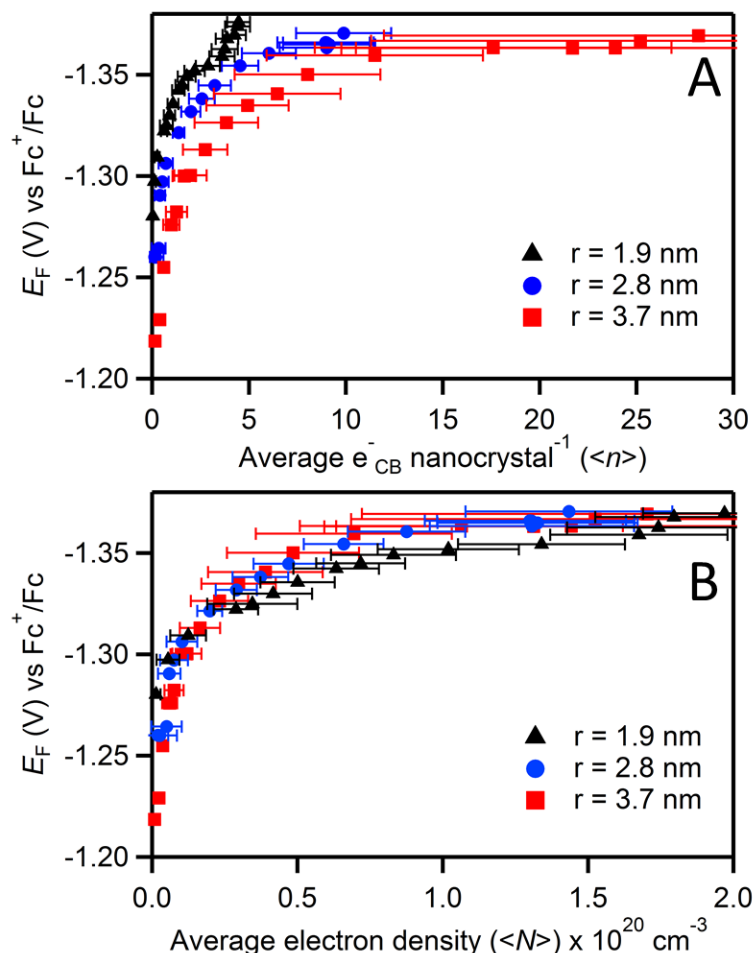


Figure 2. (A) E_F values for $r = 1.9 \text{ nm}$ ($5 \mu\text{M}$, black triangles), 2.8 nm ($8 \mu\text{M}$, blue circles), and 3.7 nm ($6 \mu\text{M}$, red squares) ZnO nanocrystals photodoped with ethanol, plotted vs $\langle n \rangle$. (B) The same E_F data plotted vs average electron density ($\langle N \rangle$). E_F values are referenced to the ferrocenium/ferrocene (Fc^+/Fc) redox couple.

It is important to note that all values of $\langle N \rangle$ and E_F reported here have been measured in the absence of ZnO UV photoexcitation. Under these conditions, and when rigorously anaerobic, $\langle N \rangle$ and E_F (or $\langle N_{\text{max}} \rangle$ and E_F^{max}) remain constant for very long times (*e.g.*, $k_{\text{decay}} < \sim 0.01/\text{week}$ at 298 K).⁵ Kinetic contributions to $\langle N \rangle$ and E_F are observed under continuous UV photoexcitation, of course, where their precise steady-state (photostationary) values depend on the ZnO photoexcitation rate. Under illumination, steady-state values of $\langle N \rangle$ can exceed $\langle N_{\text{max}} \rangle$, and electron quasi-Fermi levels can exceed E_F^{max} (see Supporting Information). Upon

1
2
3 termination of the UV illumination, however, $\langle N \rangle$ and E_F both relax quickly in the dark to
4
5 $\langle N_{\max} \rangle$ and E_F^{\max} , at which point they are stable. Resuming the UV illumination again raises
6
7
8 $\langle N \rangle$ and E_F to some steady-state values that depend on the UV irradiation parameters, but after
9
10 terminating the UV illumination they again return to the same $\langle N_{\max} \rangle$ and E_F^{\max} (see Supporting
11
12 Information). $\langle N_{\max} \rangle$ and E_F^{\max} are thus independent of the ZnO photoexcitation parameters.
13
14 These observations strongly support the conclusion that $\langle N_{\max} \rangle$ and E_F^{\max} are determined
15
16 thermodynamically, not kinetically.
17
18

19
20 We propose that the limit to E_F^{\max} arises from the existence of a side redox reaction that
21
22 occurs spontaneously at more reducing values of E_F . Specifically, we propose that E_F^{\max} (and
23
24 hence $\langle N_{\max} \rangle$ and also $\langle n_{\max} \rangle$) under the present photodoping reaction conditions is pinned by
25
26 the reversibility of the EtOH oxidation reaction, *i.e.*, by the spontaneous two-electron/two-proton
27
28 transfer from heavily reduced ZnO nanocrystals to acetaldehyde. This back reaction should occur
29
30 at the same potential regardless of the nanocrystal radius, consistent with the size-independent
31
32 E_F^{\max} observed in Figure 2. Experimentally, detection of EtOH formed from the proposed back
33
34 reaction is not trivial, so to test the hypothesis of aldehyde hydrogenation by photoreduced ZnO
35
36 nanocrystals, two sets of experiments were performed that indirectly probe the role of
37
38 acetaldehyde. In the first, ZnO nanocrystals were photodoped to $\langle N_{\max} \rangle$ in the presence of
39
40 different amounts of added acetaldehyde. Figure 3 reveals that $\langle N_{\max} \rangle$ decreases nearly linearly
41
42
43
44
45
46 with added acetaldehyde, consistent with the hypothesized aldehyde hydrogenation chemistry.
47
48
49
50
51
52
53
54
55
56
57
58
59
60

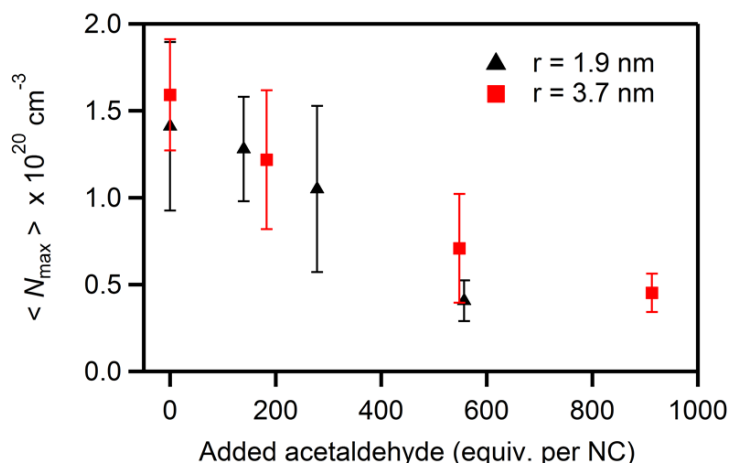


Figure 3. Maximum average electron densities ($\langle N_{\max} \rangle$) achievable in colloidal ZnO nanocrystals photoreduced using EtOH as the hole scavenger, measured in the presence of added acetaldehyde. Data for $r = 1.9 \text{ nm}$ (5 μM , black triangles) and 3.7 nm (6 μM , red squares) ZnO nanocrystals are plotted. The error bars indicate $\pm\sigma$ from $\langle N \rangle$.

In the second, benzaldehyde was used as a surrogate for acetaldehyde. In these experiments, ZnO nanocrystals were photodoped using EtOH as described above, but now in the presence of added benzaldehyde (see Supporting Information). Hydrogenation of benzaldehyde generates benzyl alcohol, which can be identified by its characteristic ^1H NMR peak at 4.2 ppm (vs TMS) arising from its $\alpha\text{-CH}_2$ protons. ^1H NMR spectroscopy thus offers a convenient and sensitive probe of this chemistry. Figure 4a plots ^1H NMR data collected after various durations of UV illumination under the normal photodoping conditions, but now in the presence of added benzaldehyde. $\langle N_{\max} \rangle$ is reached after $\sim 45 \text{ min}$ of UV excitation in these measurements (see Supporting Information), but over longer illumination times the formation of benzyl alcohol becomes evident from the appearance and growth of the broad $\alpha\text{-CH}_2$ signal at 4.22 ppm, accompanied by a concomitant decrease in the intensity of the $\alpha\text{-CH}$ signal of benzaldehyde at 9.63 ppm. The broadening of the 4.2 ppm signal relative to that of neat benzyl alcohol (see Supporting Information) is likely due to association of the benzyl alcohol with the ZnO surface³²

1
2
3 or surface-capping ligands. Figure 4b plots integrated benzaldehyde and benzyl alcohol NMR
4
5 intensities as a function of UV illumination time, showing that the changes in the concentrations
6
7 of these two species are inversely correlated. Benzyl alcohol formation was confirmed by GC-
8
9 MS. Importantly, benzyl alcohol is not formed under the same conditions when benzaldehyde is
10
11 irradiated by extensive UV illumination in the absence of the ZnO nanocrystals (see Supporting
12
13 Information). We thus conclude that photoreduced ZnO nanocrystals can indeed hydrogenate
14
15 aldehydes to form alcohols. Combined with the data from Figure 3, these results provide strong
16
17 support for the conclusion that acetaldehyde hydrogenation is responsible for Fermi-level
18
19 pinning during ZnO photodoping when using EtOH as the hole quencher, explaining at a
20
21 microscopic level one of the more striking features of this nanocrystal redox chemistry.
22
23
24
25
26
27
28
29
30
31
32
33
34
35
36
37
38
39
40
41
42
43
44
45
46
47
48
49
50
51
52
53
54
55
56
57
58
59
60

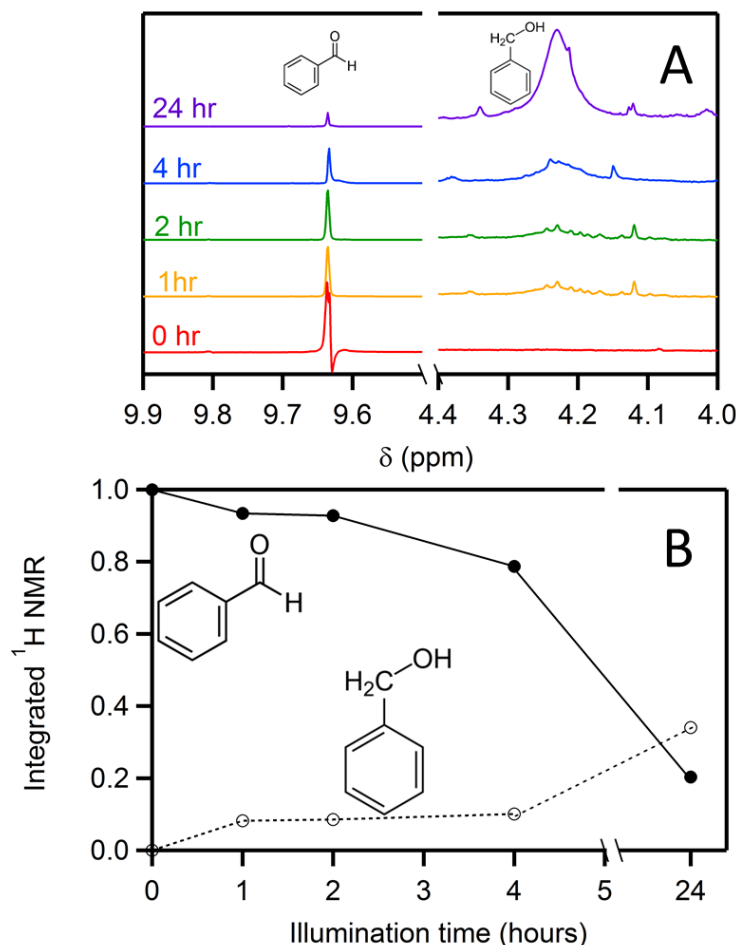


Figure 4. (A) ¹H NMR spectra (500 MHz) of TOPO-capped ZnO nanocrystals ($r = 1.9$ nm, $94 \mu\text{M}$) in 1:3 toluene-*d*₈/benzene-*d*₆ spiked with ethanol and benzaldehyde in $\sim 10^4\times$ excess (per ZnO NC) at 0 hr (red), 1 hr (yellow), 2 hr (green), 4 hr (blue), and 24 hr (violet) of UV illumination. Control measurements show no benzyl alcohol formation under UV irradiation in the absence of the ZnO nanocrystals (see Supporting Information). For clarity, the spectra are offset vertically and each side is normalized to the TOPO ligand signal at 2.5 ppm (not shown, see Supporting Information). (B) Integrated intensities of the α -CH benzaldehyde (9.8 ppm) and α -CH₂ benzyl alcohol (4.3 ppm) ¹H NMR signals relative to the TOPO CH₂ signal (2.5 ppm). These data are normalized to the benzaldehyde integrated intensity at 0 hours. The presence of two α -CH₂ protons per benzyl alcohol was accounted for by halving the total normalized intensity for this signal. For reference, $\langle N_{\text{max}} \rangle$ is reached after ~ 45 min of UV excitation in these measurements.

Finally, we address the influence of charge-compensating cations on E_{F} . Charge-compensating cations play an integral role in the formation, stabilization, and reactivity of

reduced ZnO nanocrystals.^{6,16,31} In particular, protons greatly facilitate the reduction of ZnO NCs electrochemically³¹ and by chemical reductants,¹⁶ displaying exceptional effectiveness in stabilizing reduced ZnO nanocrystals relative to bulkier cations. To quantify the effects of protons, E_F values were measured for colloidal $r = 1.9$ nm ZnO nanocrystals reduced either photochemically (using EtOH) or chemically (using Cp^*Co). Figure 5 summarizes these results. Strikingly, E_F is nearly 600 meV more negative for the chemically reduced nanocrystals than for the photodoped nanocrystals, and photodoping can introduce more than four times as many CB electrons as achieved by chemical reduction under these conditions. If E_F were determined solely by factors intrinsic to ZnO, such as the initial one-electron orbital energies or unscreened electron-electron repulsion, no difference in E_F would be observed with different reductants. The data in Figure 5 thus demonstrate and quantify the very large difference between CB electrons stabilized by H^+ and those stabilized by Cp^*Co^+ .

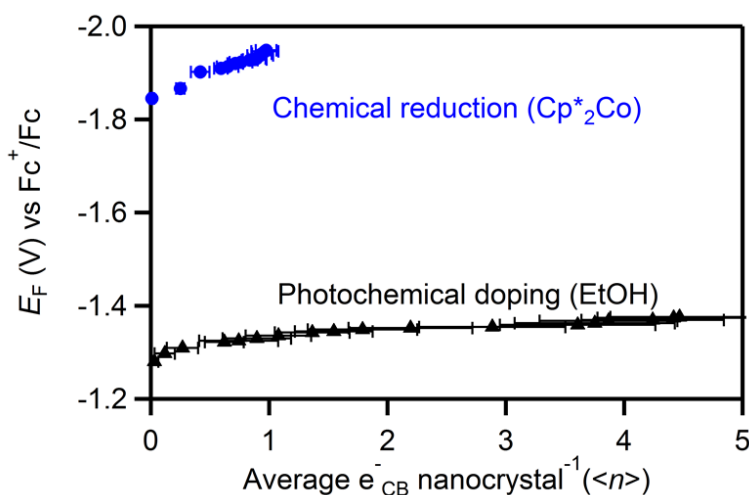
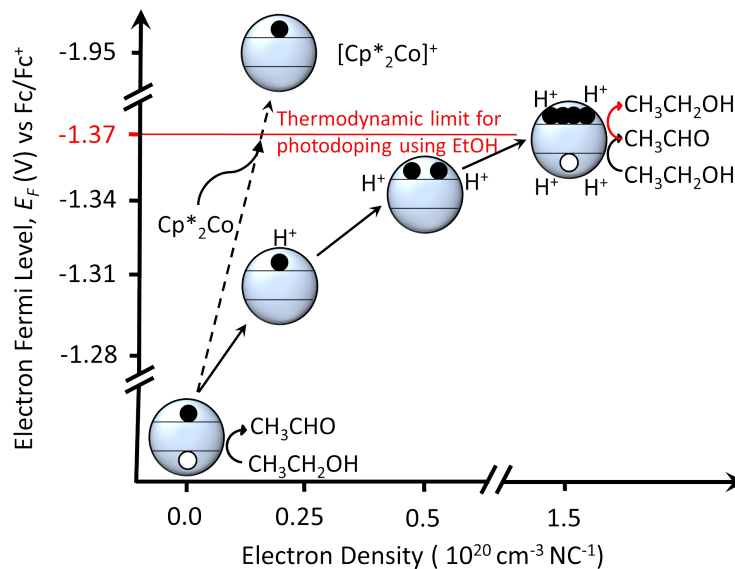


Figure 5. Comparison of E_F values measured for colloidal ZnO nanocrystals ($r = 1.9$ nm) reduced chemically using Cp^*Co (blue circles) and photochemically using EtOH (black triangles), both measured using the $\text{Cp}_2\text{Co}^+/\text{Cp}_2\text{Co}$ couple as an optical redox indicator. The error bars indicate $\pm\sigma$ from the average value of $\langle n \rangle$.

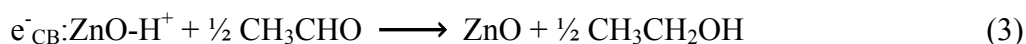
Discussion

Scheme 1 summarizes the changes in ZnO nanocrystal Fermi level during progressive photodoping using EtOH as the hole quencher and relates them to the changes observed upon chemical reduction by electron transfer from Cp^*Co . For the same nanocrystals reduced photochemically and chemically, comparison of E_F values measured at $\langle n \rangle = 1$ (Figure 5) reveals that electrons compensated by H^+ are nearly 600 meV more stable than those compensated by Cp^*Co^+ , a remarkably large difference. This difference could arise from more effective Coulombic stabilization (screening) of CB electrons by protons than by the bulky Cp^*Co^+ counter ions, especially if protons are able to diffuse into the internal volumes of the nanocrystals, but it likely also reflects the formation of a strong O–H bond upon nanocrystal reduction using EtOH. Formation of a strong ZnO–H bond stabilizes the reduced nanocrystal product, lowers the electron's chemical potential, and in turn allows greater maximum electron densities to be attained in the same ZnO nanocrystals via photodoping than via reduction by Cp^*Co .

Scheme 1



With extended photodoping (eq 1), E_F becomes dominated by electron-electron repulsive interactions that scale with electron density, yielding a single relationship between E_F and $\langle N \rangle$ that holds for all nanocrystal sizes. Between $\langle N \rangle = 2 \times 10^{19} \text{ cm}^{-3}$ and $5 \times 10^{19} \text{ cm}^{-3}$, E_F rises with a slope of ca. $-130 \text{ meV}/(10^{20} \text{ cm}^{-3})$, but subsequently shows asymptotic behavior indicative of Fermi-level pinning. The microscopic origin of the Fermi-level pinning has been identified as the acetaldehyde hydrogenation reaction, which at low electron densities is negligible but becomes more favorable as E_F increases. When E_F reaches ca. -1.37 V vs Fc^+/Fc (E_F^{max}), at $\langle N_{\text{max}} \rangle = \sim 1.6 \times 10^{20} \text{ cm}^{-3}$, UV illumination yields no further stable electron accumulation within the ZnO nanocrystals. At this point, further EtOH photooxidation is followed by spontaneous (dark) aldehyde hydrogenation (eq 3). The E_F^{max} values reported here are thus dictated by the dark reverse reaction of eq 1.



It is possible that this reaction continues on an imperceptibly slow timescale ($> \text{days}$) after its apparent equilibration within seconds or minutes. Strictly speaking, these photodoped nanocrystals would then be kinetically stable but not truly at equilibrium. This scenario could arise from proton diffusion. For example, it is possible that the correct proton configurations at the nanocrystal surfaces do not exist in these reduced nanocrystals because of proton diffusion into the internal nanocrystal volumes, driven by the greater electron density within the nanocrystal cores and by proton-proton repulsion in they types of structures with two proximal protons that might be required for aldehyde hydrogenation. At this time, the details of this reaction remain poorly understood. Clarification of such details will be the focus of future studies with this system.

Heterogeneous catalytic hydrogenation of aldehydes by ZnO has been reported

1
2
3 previously, but the reaction generally takes place at elevated temperature (~ 650 K) under
4 continuous H_2 flow,^{32,33} or requires a noble metal co-catalyst,³⁴ and it is not driven by photons.
5 Here, aldehyde hydrogenation occurs as the result of a very negative E_F in ZnO achieved by
6 extensive nanocrystal photoreduction. Although further analysis of this aldehyde hydrogenation
7 reactivity is beyond the scope of the present study, this observation of multi-electron/multi-
8 proton chemistry involving heavily reduced semiconductor nanocrystals generated
9 photochemically could have interesting implications in the area of solar fuels.^{35,36}

10
11 Finally, recent work has demonstrated analogous photodoping of colloidal In_2O_3
12 nanocrystals using EtOH as the hole quencher,⁷ as well as photodoping of ZnO^6 and CdE (E = S,
13 Se, Te)⁸ nanocrystals with a variety of hydride hole quenchers (*e.g.*, $Li[Et_3BH]$). Although
14 beyond the scope of the present study, it is interesting to consider the possibility that Fermi-level
15 pinning might also be responsible for the maximum photodoping levels observed in these
16 nanocrystals. In_2O_3 is most similar to ZnO. In_2O_3 nanocrystals can be photodoped using EtOH to
17 comparable maximum electron densities as in ZnO nanocrystals, which would be consistent with
18 a similar limiting mechanism, but the different surface chemistries of In_2O_3 and ZnO
19 nanocrystals can reasonably be anticipated to lead to different hydrogenation catalysis and hence
20 different limiting Fermi levels. In contrast with ZnO nanocrystals, CdE nanocrystals often have
21 mid-gap surface electron traps that may impact photodoping, and these nanocrystals also do not
22 form strong bonds with protons, suggesting unrelated redox chemistries may instead dominate.
23 Overall, while the specific redox processes described here for ZnO may not be central in these
24 other photodoping chemistries, the concept of photodoping limited by competing redox reactions
25 rather than by photophysical recombination kinetics may be general. Future studies on
26 photodoping involving these other materials will address these interesting open questions.
27
28
29
30
31
32
33
34
35
36
37
38
39
40
41
42
43
44
45
46
47
48
49
50
51
52
53
54
55
56
57
58
59
60

Conclusion

A simple optical method employing a solvated redox indicator has been applied for *in situ* determination of reduced ZnO nanocrystal redox potentials. These measurements reveal that the Fermi levels of solutions of nanocrystals possessing an average of just one CB electron per nanocrystal can vary by over 600 meV depending upon the method of charge compensation, and also reveal electron quantum-confinement effects for a fixed charge-compensating cation (H^+) but different nanocrystal sizes. For ZnO nanocrystals photodoped using EtOH as the hole quencher, the Fermi level becomes independent of nanocrystal size at average electron densities of $\sim 2 \times 10^{19} \text{ cm}^{-3}$. The maximum carrier densities achievable via photodoping, $\sim 2 \times 10^{20} \text{ cm}^{-3}$, are found to be determined by electron Fermi-level pinning. Microscopically, this Fermi-level pinning is identified as arising from the spontaneous two-electron two-proton hydrogenation of acetaldehyde, which reverses the EtOH photooxidation reaction. This hydrogenation reaction, and hence the maximum nanocrystal photodoping level, occurs at the same potential for all nanocrystal sizes, explaining the microscopic basis for the maximum electron densities achievable via this photochemistry.

Supporting Information Available

Additional experimental results (10 figures). This information is available free of charge *via* the internet at <http://pubs.acs.org>.

Acknowledgments. This research was supported financially by the U.S. National Science Foundation (CHE-1151726 and CHE-1506014 to D.R.G., Graduate Research Fellowship DGE-1256082 to A.M.S.), the U.S. National Institutes of Health (Postdoctoral Fellowship F32GM110876 to E.Y.T.), and the University of Washington Clean Energy Institute. The authors gratefully acknowledge Prof. James Mayer for fruitful discussions.

References

- (1) Haase, M.; Weller, H.; Henglein, A. *J. Phys. Chem.* **1988**, *92*, 482-487.
- (2) Shim, M.; Guyot-Sionnest, P. *J. Am. Chem. Soc.* **2001**, *123*, 11651-11654.
- (3) Wood, A.; Giersig, M.; Mulvaney, P. *J. Phys. Chem. B* **2001**, *105*, 8810-8815.

- (4) Germeau, A.; Roest, A. L.; Vanmaekelbergh, D.; Allan, G.; Delerue, C.; Meulenkamp, E. A. *Phys. Rev. Lett.* **2003**, *90*, 097401.
- (5) Liu, W. K.; Whitaker, K. M.; Kittilstved, K. R.; Gamelin, D. R. *J. Am. Chem. Soc.* **2006**, *128*, 3910-3911.
- (6) Schimpf, A. M.; Gunthardt, C. E.; Rinehart, J. D.; Mayer, J. M.; Gamelin, D. R. *J. Am. Chem. Soc.* **2013**, *135*, 16569-16577.
- (7) Schimpf, A. M.; Lounis, S. D.; Runnerstrom, E. L.; Milliron, D. J.; Gamelin, D. R. *J. Am. Chem. Soc.* **2015**, *137*, 518-524.
- (8) Rinehart, J. D.; Schimpf, A. M.; Weaver, A. L.; Cohn, A. W.; Gamelin, D. R. *J. Am. Chem. Soc.* **2013**, *135*, 18782-18785.
- (9) Cohn, A. W.; Janßen, N.; Mayer, J. M.; Gamelin, D. R. *J. Phys. Chem. C* **2012**, *116*, 20633-20642.
- (10) Markham, M. C.; Hannan, M. C.; Paternostro, R. M.; Rose, C. B. *J. Am. Chem. Soc.* **1958**, *80*, 5394-5397.
- (11) Cunningham, J.; Hodnett, B. K. *J. Chem. Soc., Faraday Trans. 1* **1981**, *77*, 2777-2801.
- (12) van Dijken, A.; Meulenkamp, E. A.; Vanmaekelbergh, D.; Meijerink, A. *J. Lumin.* **2000**, *90*, 123-128.
- (13) Wood, A.; Giersig, M.; Hilgendorff, M.; Vilas-Campos, A.; Liz-Marzán, L. M.; Mulvaney, P. *Aust. J. Chem.* **2003**, *56*, 1051-1057.
- (14) Hayoun, R.; Whitaker, K. M.; Gamelin, D. R.; Mayer, J. M. *J. Am. Chem. Soc.* **2011**, *133*, 4228-4231.
- (15) Cohn, A. W.; Kittilstved, K. R.; Gamelin, D. R. *J. Am. Chem. Soc.* **2012**, *134*, 7937-7943.
- (16) Valdez, C. N.; Braten, M.; Soria, A.; Gamelin, D. R.; Mayer, J. M. *J. Am. Chem. Soc.* **2013**, *135*, 8492-8495.
- (17) Schwartz, D. A.; Norberg, N. S.; Nguyen, Q. P.; Parker, J. M.; Gamelin, D. R. *J. Am. Chem. Soc.* **2003**, *125*, 13205-13218.
- (18) Norberg, N. S.; Gamelin, D. R. *J. Phys. Chem. B* **2005**, *109*, 20810-20816.
- (19) Meulenkamp, E. A. *J. Phys. Chem. B* **1998**, *102*, 5566-5572.
- (20) Schimpf, A. M.; Ochsenbein, S. T.; Buonsanti, R.; Milliron, D. J.; Gamelin, D. R. *Chem. Commun.* **2012**, *48*, 9352-9354.
- (21) Schrauben, J. N.; Hayoun, R.; Valdez, C. N.; Braten, M.; Fridley, L.; Mayer, J. M. *Science* **2012**, *336*, 1298-1301.
- (22) Gordon, K. R.; Warren, K. D. *Inorg. Chem.* **1978**, *17*, 987-994.
- (23) Liu, W. K.; Whitaker, K. M.; Smith, A. L.; Kittilstved, K. R.; Robinson, B. H.; Gamelin, D. R. *Phys. Rev. Lett.* **2007**, *98*, 186804.
- (24) Schimpf, A. M.; Thakkar, N.; Gunthardt, C. E.; Masiello, D. J.; Gamelin, D. R. *ACS Nano* **2013**, *8*, 1065-1072.
- (25) Shim, M.; Guyot-Sionnest, P. *Nature* **2000**, *407*, 981-983.
- (26) Goings, J. J.; Schimpf, A. M.; May, J. W.; Johns, R. W.; Gamelin, D. R.; Li, X. *J. Phys. Chem. C* **2014**, *118*, 26584-26590.
- (27) Reiss, H. *J. Phys. Chem.* **1985**, *89*, 3783-3791.
- (28) Khan, S. U. M.; Kainthla, R. C.; Bockris, J. O. M. *J. Phys. Chem.* **1987**, *91*, 5974-5977.
- (29) Roest, A. L.; Kelly, J. J.; Vanmaekelbergh, D.; Meulenkamp, E. A. *Phys. Rev. Lett.* **2002**, *89*, 036801.
- (30) Connelly, N. G.; Geiger, W. E. *Chem. Rev.* **1996**, *96*, 877-910.
- (31) Roest, A. L.; Germeau, A.; Kelly, J. J.; Vanmaekelbergh, D.; Allan, G.; Meulenkamp, E. A.

ChemPhysChem **2003**, *4*, 959-966.

(32) Haffad, D.; Kameswari, U.; Bettahar, M. M.; Chambellan, A.; Lavalley, J. C. *J. Catal.* **1997**, *172*, 85-92.

(33) Bowker, M.; Houghton, H.; Waugh, K. C. *J. Phys. Chem. Soc., Faraday Trans.* **1982**, *78*, 2573-2582.

(34) Mäki-Arvela, P.; Hájek, J.; Salmi, T.; Murzin, D. Y. *Appl. Catal. A* **2005**, *292*, 1-49.

(35) Smestad, G. P.; Steinfeld, A. *Indus. Eng. Chem. Res.* **2012**, *51*, 11828-11840.

(36) Rausch, B.; Symes, M. D.; Chisholm, G.; Cronin, L. *Science* **2014**, *345*, 1326-1330.

TOC Graphic

